

Fundamental Limits on Energy-Delay-Accuracy of In-memory Architectures in Inference Applications

Sujan K. Gonugondla *Member, IEEE*, Charbel Sakr *Graduate Student Member, IEEE*,
Hassan Dbouk *Student Member, IEEE*, and Naresh R. Shanbhag *Fellow, IEEE*

Abstract—This paper obtains fundamental limits on the computational precision of in-memory computing architectures (IMCs). An IMC noise model and associated SNR metrics are defined and their interrelationships analyzed to show that the accuracy of IMCs is fundamentally limited by the compute SNR (SNR_a) of its analog core, and that activation, weight and output precision needs to be assigned appropriately for the final output SNR $\text{SNR}_T \rightarrow \text{SNR}_a$. The minimum precision criterion (MPC) is proposed to minimize the ADC precision. Three in-memory compute models - charge summing (QS), current summing (IS) and charge redistribution (QR) - are shown to underlie most known IMCs. Noise, energy and delay expressions for the compute models are developed and employed to derive expressions for the SNR, ADC precision, energy, and latency of IMCs. The compute SNR expressions are validated via Monte Carlo simulations in a 65 nm CMOS process. For a 512 row SRAM array, it is shown that: 1) IMCs have an upper bound on their maximum achievable SNR_a due to constraints on energy, area and voltage swing, and this upper bound reduces with technology scaling for QS-based architectures; 2) MPC enables $\text{SNR}_T \rightarrow \text{SNR}_a$ to be realized with minimal ADC precision; 3) QS-based (QR-based) architectures are preferred for low (high) compute SNR scenarios.

I. INTRODUCTION

In-memory computing (IMC) [1]–[4] has emerged as an attractive alternative to conventional von Neumann (digital) architectures for addressing the energy and latency cost of memory accesses in data-centric machine learning workloads. IMCs embed analog mixed-signal computations in close proximity to the bit-cell array (BCA) in order to execute machine learning computations such as matrix-vector multiply (MVM) and dot products (DPs) as an intrinsic part of the read cycle and thereby avoid the need to access raw data.

IMCs exhibit a fundamental trade-off between its energy-delay product (EDP) and the accuracy or *signal-to-noise ratio* (SNR) of its analog computations. This trade-off arises due to constraints on the maximum bit-line (BL) voltage discharge and due to process variations, specifically spatial variations in the threshold voltage V_t , which limit the dynamic range and the SNR. Additionally, IMCs also exhibit noise due to the quantization of its input activation and weight parameters and due to the column analog-to-digital converters (ADCs).

Charbel Sakr, Hassan Dbouk, and Naresh R. Shanbhag are with the Department of Electrical and Computer Engineering, at the University of Illinois at Urbana-Champaign.

Sujan K. Gonugondla is with Amazon in Seattle, Washington. This work was done during his time at the University of Illinois at Urbana-Champaign.

This work was supported by C-BRIC, one of six centers in JUMP, a Semiconductor Research Corporation (SRC) program sponsored by DARPA. We thank Professor Boris Murmann for helpful discussions and suggestions.

Henceforth, we use “compute SNR” to refer to the computational precision/accuracy of an IMC, and “precision” to the number of bits assigned to various signals.

Today, a large number of IMC prototype ICs and designs have been demonstrated [5]–[27]. While these IMCs have shown impressive reductions in the EDP over a von Neumann equivalent with minimal loss in inference accuracy, it is not clear that these gains are sustainable for larger problem sizes across data sets and inference tasks. Unlike digital architectures whose compute SNR can be made arbitrarily high by assigning sufficiently high precision to various signals, IMCs need to contend with both quantization noise as well as analog non-idealities. Therefore, IMCs will have intrinsic limits on their compute SNR. Since the compute SNR trades-off with energy and delay, it raises the following question: *What are the fundamental limits on the achievable computational precision of IMCs?*

Answering this question is made challenging due to the rich design space occupied by IMCs encompassing a huge diversity of available memory devices, bitcell circuit topologies, circuit and architectural design methods. Today’s IMCs tend to employ ad-hoc approaches to assign input and ADC precisions or tend to overprovision its analog SNR in order to emulate the determinism of digital computations.

Recently in [28], we have attempted to answer the above question for the specific IMC in [6]. A comprehensive analytical understanding of the relationship between precision, compute SNR, energy, and delay across all types of IMCs, is presently missing. This paper fills this gap (preliminary results in [29]) by: 1) defining compute SNR metrics for IMCs, 2) developing a systematic methodology to obtain a minimum precision assignment for activations, weights and outputs of fixed-point DPs realized on IMCs to meet network accuracy requirements, and 3) employing this methodology to obtain the limits on achievable compute SNR of commonly employed IMC topologies, and quantify their energy vs. accuracy trade-offs.

This paper is organized as follows: Section II presents preliminaries related to signal and DP quantization. Section III proposes the IMC noise model and associated compute SNR metrics. Section IV presents analytical expressions for the compute SNR of three different IMCs. Simulation results quantifying various trade-offs including those between energy and accuracy are presented in Section V. Section VI summarizes the key takeaways for designing IMCs.

II. NOTATION AND PRELIMINARIES

A. General Notation

We employ the term signal-to-quantization noise ratio (SQNR) when *only* quantization noise (denoted as q) is involved. The term SNR is employed when analog noise sources are included and use η to denote such sources. SNR is also employed when both quantization and analog noise sources are present.

B. The Additive Quantization Noise Model

Under the additive quantization noise model, a floating-point (FL) signal x quantized to B_x bits is represented as $x_q = x + q_x$, where q_x is the quantization noise assumed to be independent of the signal x .

If $x \in [-x_m, x_m]$ and $q_x \sim U[-0.5\Delta_x, 0.5\Delta_x]$ where $\Delta_x = x_m 2^{-(B_x-1)}$ is the quantization step size and $U[a, b]$ denotes the uniform distribution over the interval $[a, b]$, then the signal-to-quantization noise ratio (SQNR $_x$) is given by:

$$\text{SQNR}_{x(\text{dB})} = 10 \log_{10}(\text{SQNR}_x) = 6B_x + 4.78 - \zeta_{x(\text{dB})} \quad (1)$$

where $\text{SQNR}_x = \frac{\sigma_x^2}{\sigma_{q_x}^2}$, $\sigma_{q_x}^2 = \frac{\Delta_x^2}{12}$, and $\zeta_x(\text{dB}) = 10 \log_{10}(\frac{x_m^2}{\sigma_x^2})$ is the peak-to-average (power) ratio (PAR) of x . Equation (1) quantifies the familiar 6 dB SQNR gain per bit of precision.

C. The Dot-Product (DP) Computation

Consider the FL dot product (DP) computation defined as:

$$y_o = \mathbf{w}^T \mathbf{x} = \sum_{j=1}^N w_j x_j \quad (2)$$

where y_o is the DP of two N -dimensional real-valued vectors $\mathbf{w} = [w_1, \dots, w_N]^T$ (weight vector) and $\mathbf{x} = [x_1, \dots, x_N]^T$ (activation vector).

In DNNs, the dot product in (2) is computed with $w \in [-w_m, w_m]$ (signed weights), input $x \in [0, x_m]$ (unsigned activations assuming the use of ReLU activation functions) and output $y \in [-y_m, y_m]$ (signed outputs). Assuming the additive quantization noise model from Section II-B, the fixed-point (FX) computation of the DP (2) with precisions B_w (weight), B_x (activation), and B_y (output), is described by:

$$y = \mathbf{w}_q^T \mathbf{x}_q + q_y = (\mathbf{w} + \mathbf{q}_w)^T (\mathbf{x} + \mathbf{q}_x) + q_y \quad (3)$$

$$\approx \mathbf{w}^T \mathbf{x} + \mathbf{w}^T \mathbf{q}_x + \mathbf{q}_w^T \mathbf{x} + q_y = y_o + q_{iy} + q_y \quad (4)$$

where $\mathbf{w}_q = \mathbf{w} + \mathbf{q}_w$ and $\mathbf{x}_q = \mathbf{x} + \mathbf{q}_x$ are the quantized weight and activation vectors, respectively, q_{iy} is the total input (weight and activation) quantization noise seen at the output y (output referred quantization noise), and q_y is the additional output quantization noise due to round-off/truncation in digital architectures or from the finite resolution of the column ADCs in IMC architectures.

Assuming that the weights (signed) and inputs (unsigned) are i.i.d. random variables (RVs), the variances of signals in (4) are given by:

$$\sigma_{y_o}^2 = N \sigma_w^2 \mathbb{E}[x^2]; \sigma_{q_y}^2 = \frac{\Delta_y^2}{12}; \sigma_{q_{iy}}^2 = \frac{N}{12} (\Delta_w^2 \mathbb{E}[x^2] + \Delta_x^2 \sigma_w^2) \quad (5)$$

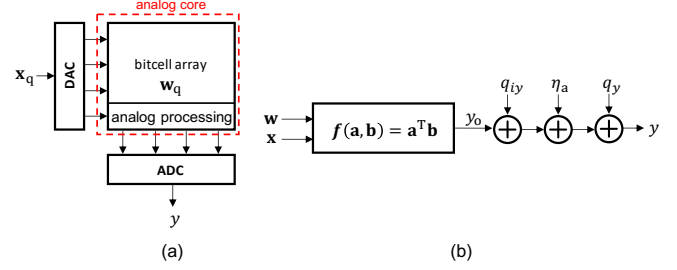


Fig. 1. System noise model of IMC: (a) a generic IMC block diagram, and (b) dominant noise sources in a fixed-point DP computation on IMCs.

where σ_w^2 is the variance of the weights, $\Delta_w = w_m 2^{-B_w+1}$, $\Delta_x = x_m 2^{-B_x}$ and $\Delta_y = y_m 2^{-B_y+1}$ are the weight, activation, and output quantization step-sizes, respectively.

III. COMPUTE SNR LIMITS OF IMCS

We propose the system noise model in Fig. 1 for obtaining precision limits on IMCs. Such architectures (Fig. 1(a)) accept a quantized input (\mathbf{x}_q) and a quantized weight vector (\mathbf{w}_q) to implement multiple FX DP computations of (4) in parallel in its analog core. Hence, unlike digital architectures, IMC architectures suffer from both quantization and analog noise sources such as SRAM cell current variations, thermal noise, and charge injection, as well as the limited headroom, which limits its compute SNR.

A. Compute SNR Metrics for IMCs

The following equations describe the IMC noise model in Fig. 1:

$$y = y_o + q_{iy} + \eta_a + q_y; \quad \eta_a = \eta_e + \eta_h \quad (6)$$

where y_o is the ideal DP value defined in (2), q_{iy} is the output referred quantization noise, η_a is the analog noise term comprising both clipping noise η_h due to limited headroom and other noise sources η_e , and q_y is the output quantization noise introduced by the ADC.

We define the following fundamental compute SNR metrics:

$$\text{SQNR}_{q_{iy}} = \frac{\sigma_{y_o}^2}{\sigma_{q_{iy}}^2}; \text{SNR}_a = \frac{\sigma_{y_o}^2}{\sigma_{\eta_a}^2}; \text{SQNR}_{q_y} = \frac{\sigma_{y_o}^2}{\sigma_{q_y}^2} \quad (7)$$

where SNR_a is the *analog SNR*, $\text{SQNR}_{q_{iy}}$ is the *output referred SQNR* due to input (weight and activation) quantization and is given by:

$$\text{SQNR}_{q_{iy}(\text{dB})} = 6(B_x + B_w) + 4.8 - [\zeta_{x(\text{dB})} + \zeta_{w(\text{dB})}] - 10 \log_{10} \left(\frac{2^{2B_x}}{\zeta_x^2} + \frac{2^{2B_w}}{\zeta_w^2} \right) \quad (8)$$

where $\zeta_x(\text{dB}) = 10 \log_{10} \left(\frac{x_m^2}{4 \mathbb{E}[x^2]} \right)$ and $\zeta_w(\text{dB}) = 10 \log_{10} \left(\frac{w_m^2}{\sigma_w^2} \right)$ are the PARs of the (unsigned) activations and (signed) weights, respectively, and SQNR_{q_y} is the *digitization SQNR* solely due to ADC quantization noise and is given by:

$$\text{SQNR}_{q_y(\text{dB})} = 6B_y + 4.8 - [\zeta_{x(\text{dB})} + \zeta_{w(\text{dB})}] - 10 \log_{10}(N) \quad (9)$$

obtained by the substitutions: $B_x \leftarrow B_y$ and $\zeta_{x(\text{dB})} \leftarrow \zeta_{y(\text{dB})} = \zeta_{x(\text{dB})} + \zeta_{w(\text{dB})} + 10 \log_{10}(N)$ in (1).

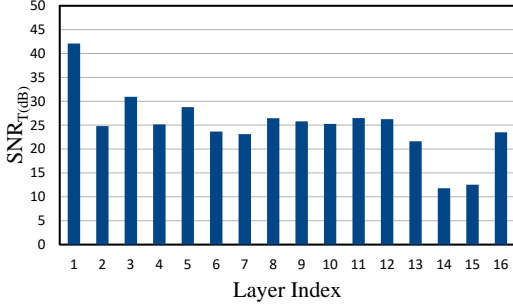


Fig. 2. Per-layer $\text{SNR}_{\text{T}(\text{dB})}$ requirements of DP computations in VGG-16 deployed on ImageNet.

From (6) and (7), it is straightforward to show:

$$\text{SNR}_{\text{A}} = \frac{\sigma_{y_o}^2}{\sigma_{q_{iy}}^2 + \sigma_{\eta_a}^2} = \left[\frac{1}{\text{SNR}_{\text{a}}} + \frac{1}{\text{SQNR}_{q_{iy}}} \right]^{-1} \quad (10)$$

$$\text{SNR}_{\text{T}} = \frac{\sigma_{y_o}^2}{\sigma_{q_{iy}}^2 + \sigma_{\eta_a}^2 + \sigma_{q_y}^2} = \left[\frac{1}{\text{SNR}_{\text{A}}} + \frac{1}{\text{SQNR}_{q_y}} \right]^{-1} \quad (11)$$

where SNR_{A} is the pre-ADC SNR and SNR_{T} is the total output SNR including all noise sources. Note: (10)-(11) can be repurposed for digital architectures by setting $\text{SNR}_{\text{a}} \rightarrow \infty$ since quantization is the only noise source thereby implying $\text{SNR}_{\text{A}} = \text{SQNR}_{q_{iy}}$. Equations (8)-(9) indicate that $\text{SQNR}_{q_{iy}}$ and SQNR_{q_y} can be made arbitrarily large by assigning sufficiently high precision to the DP inputs (B_x and B_w) and the output (B_y). Thus, from (10)-(11), SNR_{T} in IMCs is fundamentally limited by SNR_{a} which depends on the analog noise sources as one expects.

B. Maximizing SNR_{T} in IMCs

Prior work based on post-training quantization [30], [31], indicates the requirement $\text{SNR}_{\text{T}(\text{dB})} > \text{SNR}_{\text{T}(\text{dB})}^* = 10 \text{ dB} - 40 \text{ dB}$ (see Fig. 2) for the inference accuracy of an FX network to be within 1% of the corresponding FL network for popular DNNs (AlexNet, VGG-9, VGG-16, ResNet-18) deployed on the ImageNet and CIFAR-10 datasets. While in-training quantization methods [32] can reduce these requirements, a precision of 4-b ($\sim 24 \text{ dB}$) is generally found to be [33] sufficient. To meet this $\text{SNR}_{\text{T}(\text{dB})}$ requirement, digital architectures choose B_x and B_w such that $\text{SQNR}_{q_{iy}} > \text{SNR}_{\text{T}}^*$, and then choose B_y sufficiently high to guarantee $\text{SQNR}_{q_y} \gg \text{SQNR}_{q_{iy}}$ so that $\text{SNR}_{\text{T}} \rightarrow \text{SNR}_{q_{iy}}$.

In contrast, for IMCs, we first need to ensure that $\text{SNR}_{\text{a}} > \text{SNR}_{\text{T}}^*$ so that SNR_{T} can be made to approach SNR_{a} with appropriate precision assignment. Such a precision assignment can be easily derived from (10)-(11) as shown below:

- 1) Assign sufficiently high values for B_x and B_w per (8) such that $\text{SQNR}_{q_{iy}} \gg \text{SNR}_{\text{a}}$ so that $\text{SNR}_{\text{A}} \rightarrow \text{SNR}_{\text{a}}$ per (10).
- 2) Assign sufficiently a high value for B_y such that $\text{SQNR}_{q_y} \gg \text{SNR}_{\text{A}}$ so that $\text{SNR}_{\text{T}} \rightarrow \text{SNR}_{\text{A}}$ per (11).

For example, if $\text{SQNR}_{q_{iy}(\text{dB})}, \text{SQNR}_{q_y(\text{dB})} \geq \text{SNR}_{\text{a}(\text{dB})} + 9 \text{ dB}$ then $\text{SNR}_{\text{a}(\text{dB})} - \text{SNR}_{\text{T}(\text{dB})} \leq 0.5 \text{ dB}$, i.e., $\text{SNR}_{\text{T}(\text{dB})}$ lies within

0.5 dB of $\text{SNR}_{\text{a}(\text{dB})}$. In this manner, by appropriate choices for B_x , B_w , and B_y , IMCs can be designed such that $\text{SNR}_{\text{T}} \rightarrow \text{SNR}_{\text{a}}$, which, as mentioned earlier, is the fundamental limit on SNR_{T} .

From the above discussion it is clear that the input precisions B_x and B_w are dictated by network accuracy requirements, while the output precision B_y needs to be set sufficiently high for the output quantization from becoming a significant noise contributor. To ensure that a sufficiently high value for B_y , digital architectures employ the *bit growth criterion* (BGC) described next.

C. Bit Growth Criterion (BGC)

The BGC is commonly employed to assign the output precision B_y in digital architectures [30], [34]. BGC sets B_y as:

$$B_y^{\text{BGC}} = B_x + B_w + \log_2(N) \quad (12)$$

Substituting $B_y = B_y^{\text{BGC}}$ from (12) into (9) and employing the relationship $\zeta_{y(\text{dB})} = 10 \log_{10}(N) + \zeta_{x(\text{dB})} + \zeta_{w(\text{dB})}$, the resulting SQNR due to output quantization using the BGC is given by:

$$\begin{aligned} \text{SQNR}_{q_y(\text{dB})}^{\text{BGC}} &= 10 \log_{10} \left(\frac{\sigma_{y_o}^2}{\sigma_{q_y}^2} \right) \\ &= 6(B_x + B_w) + 4.8 - [\zeta_{x(\text{dB})} + \zeta_{w(\text{dB})}] + 10 \log_{10}(N). \end{aligned} \quad (13)$$

Recall that $\text{SQNR}_{q_y}^{\text{BGC}} \gg \text{SNR}_{\text{A}}$ in order to ensure SNR_{T} is close to its upper bound. Comparing (9) and (13), we see that, for high values of DP dimensionality N , BGC is overly conservative since it assigns large values to B_y per (12). Some digital architectures truncate the LSBs to control bit growth. The SQNR of such *truncated BGC* (tBGC) can be obtained directly from (9) by setting the value of $B_y < B_y^{\text{BGC}}$.

BGC's high precision requirements is accommodated in digital architectures by increasing the precision of arithmetic units with a commensurate increase in the computational energy, latency, and activation storage costs. However, IMCs cannot afford to use this criterion since B_y is the precision of the BL ADCs which impacts its energy, latency, and area. Indeed, recent works [35] have claimed that BL ADCs dominate the energy and latency costs of IMCs. Such works employ the highly conservative BGC or tBGC to assign B_y .

In the next section, we propose an alternative to BGC and tBGC referred to the *minimum precision criterion* (MPC), that can be employed by both digital and IMC architectures to achieve a desired SQNR_{q_y} with much smaller values of B_y .

D. The Minimum Precision Criterion (MPC)

We propose MPC to reduce B_y without incurring any loss in SQNR_{q_y} compared to BGC. Unlike BGC, MPC accounts for the statistics of y_o to permit controlled amounts of *clipping* to occur. In MPC (see Fig. 3(a)), the output y_o is *clipped* to lie in the range $[-y_c, y_c]$ instead of $[-y_m, y_m]$ as in BGC (see Fig. 3(b)), where $y_c < y_m$ is the *clipping level*, and B_y bits are employed to quantize this reduced range. The *clipping*

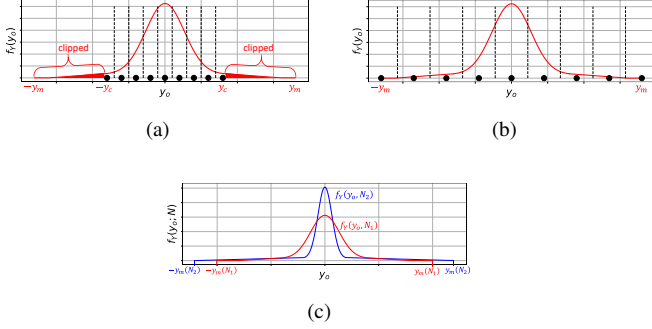


Fig. 3. Comparison of BGC and MPC: (a) MPC quantization levels, (b) BGC quantization levels, and (c) distribution $f_Y(y_o)$ of the ideal DP output y_o vs. DP dimensionality N .

probability $p_c = \Pr\{|y_o| > y_c\}$ is kept to a small user-defined value, e.g., $y_c = 4\sigma_{y_o}$ ensures that $p_c < 0.001$ if $y_o \sim \mathcal{N}(0, \sigma_{y_o}^2)$. The resulting SQNR_{q_y} is given by:

$$\text{SQNR}_{q_y(\text{dB})}^{\text{MPC}} = 6B_y + 4.8 - \zeta_{y(\text{dB})}^{\text{MPC}} - 10 \log_{10} \left(1 + p_c \frac{\sigma_{cc}^2}{\sigma_{q_y}^2} \right) \quad (14)$$

where $\zeta_{y(\text{dB})}^{\text{MPC}} = 10 \log_{10} \left(\frac{y_c^2}{\sigma_{y_o}^2} \right)$, and $\sigma_{cc}^2 = \mathbb{E}[(y_o - y_c)^2 | |y_o| > y_c]$ is the *conditional clipping noise variance*. Setting $y_c = \zeta_{y(\text{dB})}^{\text{MPC}} \sigma_{y_o}$ yields $\zeta_{y(\text{dB})}^{\text{MPC}} = 10 \log_{10} (\zeta_{y(\text{dB})}^{\text{MPC}})^2$ indicating that p_c is a decreasing function of $\zeta_{y(\text{dB})}^{\text{MPC}}$. Thus, (14) has the same form as (1) with an additional (last term) *clipping noise factor*.

MPC exploits a key insight (see Fig. 3(c)), which follows from the Central Limit Theorem (CLT) – in a N -dimensional DP computation (2), σ_{y_o} grows sub-linearly (as \sqrt{N}) as compared to the maximum y_m which grows linearly with N . Furthermore, (14) shows a *quantization vs. clipping noise trade-off* controlled by the clipping level y_c . We show empirically in Section III-E that $\text{SQNR}_{q_y(\text{dB})}^{\text{MPC}}$ in (14) is maximized when clipping level $y_c = 4\sigma_{y_o}$ if $y_o \sim \mathcal{N}(0, \sigma_{y_o}^2)$. This trade-off (see Fig. 3(b)) is absent in BGC and tBGC, and is critical to MPC's ability to realize desired values of SQNR_{q_y} with smaller values of B_y .

Thus, we state the following MPC-based rule for maximizing the SQNR of column ADCs in IMCs:

MPC-based SQNR Maximizing Rule

For a Gaussian signal, setting the clipping level to four times the standard deviation will maximize the SQNR for a given precision B_y .

Some IMC designs [36] do in fact allow for clipping in the column ADCs but these levels are set empirically. The MPC-based Rule in contrast quantitatively specifies the smallest ADC precision and the optimal clipping level needed to ensure that $\text{SQNR}_{q_y} \gg \text{SNR}_A$. A lower bound on B_y can be obtained by assuming $y_o \sim \mathcal{N}(0, \sigma_{y_o}^2)$, and substituting $y_c = 4\sigma_{y_o}$, and $p_c = 0.001$ into (14), to obtain:

$$B_y^{\text{MPC}} \geq \frac{1}{6} \left[\text{SNR}_{A(\text{dB})} + 7.2 - \gamma - 10 \log_{10} \left(1 - 10^{-\frac{\gamma}{10}} \right) \right] \quad (15)$$

in order for $\text{SNR}_{A(\text{dB})} - \text{SNR}_{T(\text{dB})} \leq \gamma$. For instance, the

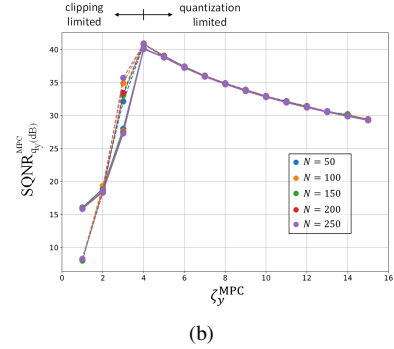
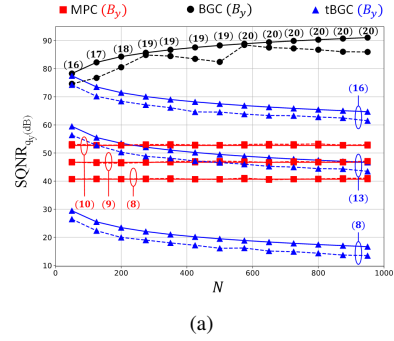


Fig. 4. Trends in $\text{SQNR}_{q_y(\text{dB})}$ for DP computation with $B_x = B_w = 7$: (a) $\text{SQNR}_{q_y(\text{dB})}$ vs. N for MPC ($\zeta_y = 4$), BGC, tBGC, and (b) $\text{SQNR}_{q_y(\text{dB})}^{\text{MPC}}$ vs. ζ_y^{MPC} when $B_y = 8$.

choice $\gamma = 0.5$ dB yields $B_y^{\text{MPC}} \geq \frac{1}{6} [\text{SNR}_{A(\text{dB})} + 16.3]$ which corresponds to $\text{SQNR}_{y(\text{dB})}^{\text{MPC}} \geq \text{SNR}_{A(\text{dB})} + 9$ dB as discussed in Section III-B.

E. Simulation Results

To illustrate the difference between MPC, BGC and tBGC, we assume that $\text{SNR}_{a(\text{dB})} \geq 31$ dB, so that $\text{SNR}_{T(\text{dB})} \geq 30$ dB provided $\text{SQNR}_{q_{i_y}(\text{dB})}, \text{SQNR}_{q_y(\text{dB})} \geq 40$ dB per (10)-(11). We further assume DPs of varying dimension N with 7-b quantized unsigned inputs and signed weights randomly sampled from uniform distributions. Substituting $B_x = B_w = 7$, $\zeta_{x(\text{dB})} = -1.3$ dB, and $\zeta_{w(\text{dB})} = 4.8$ dB into (8), we obtain $\text{SNR}_{q_{i_y}(\text{dB})} = 41$ dB. Thus, all that remains is to assign B_y such that $\text{SQNR}_{q_y(\text{dB})} \geq 40$ dB, for which there are three choices - MPC, BGC and tBGC.

Figure 4(a) compares the SQNR_{q_y} achieved by the three methods. Per (15), MPC meets the $\text{SQNR}_{q_y(\text{dB})} \geq 40$ dB requirement by setting $B_y = 8$ and $\zeta_y^{\text{MPC}} = 4$ independent of N . In contrast, per (12), BGC assigns $16 \leq B_y \leq 20$ as a monotonically increasing function of N to achieve the same SNR_T as MPC. Furthermore, tBGC meets the SQNR_{q_y} requirement with $11 \leq B_y \leq 13$ but fails to do so with $B_y = 8$. Figure 4(b) shows that $\text{SQNR}_{q_y(\text{dB})}^{\text{MPC}}$ is maximized when $\zeta_y^{\text{MPC}} = 4$, i.e., when clipping level $y_c = 4\sigma_{y_o}$ thereby illustrating MPC's quantization vs. clipping noise trade-off described by (14).

Figure 4 also validates the analytical expressions (8), (9), (13), and (14) (bold) by indicating a close match to ensemble-averaged values of SQNR_{q_y} obtained from Monte Carlo simulations (dotted).

TABLE I
A TAXONOMY OF CMOS IMC DESIGNS USING IN-MEMORY COMPUTE MODELS

	In-memory Compute Model			Analog Core Precision		ADC Precision
	QS	IS	QR	B_x	B_w	B_{ADC}
Kang <i>et al.</i> [6]	✓		✓	8	8	8
Biswas <i>et al.</i> [8]			✓	8	1	7
Zhang <i>et al.</i> [5]	✓			5	1	1
Valavi <i>et al.</i> [12]			✓	1	1	1
Khwa <i>et al.</i> [11]		✓		1	1	1
Jiang <i>et al.</i> [7]		✓		1	1	3.46
Si <i>et al.</i> [38]	✓		✓	2	5	5
Jia <i>et al.</i> [39]			✓	1	1	8
Okumura <i>et al.</i> [40]		✓		1	T	8
Kim <i>et al.</i> [13]		✓		1	1	1
Guo <i>et al.</i> [41]	✓			1	1	3
Yue <i>et al.</i> [42]	✓		✓	2	5	5
Su <i>et al.</i> [15]	✓			2	1	5
Dong <i>et al.</i> [14]	✓		✓	4	4	4
Si <i>et al.</i> [16]	✓			2	2	5
Jiang <i>et al.</i> [43]			✓	1	1	5
Jaiswal <i>et al.</i> [17]		✓		4	4	4
Ali <i>et al.</i> [18]	✓		✓	4	4	4
Si <i>et al.</i> [19]	✓			1	1	1
Liu <i>et al.</i> [20]		✓		A	1	1
Zhang <i>et al.</i> [21]		✓		8	8	8
Gong <i>et al.</i> [22]	✓			2	3	8
Agrawal <i>et al.</i> [23]			✓	1	1	5

T: Ternary; A: Analog/Continuous-valued

Note: it is well-established that the theoretically optimal quantizer given an arbitrary signal distribution is obtained from the Lloyd-Max (LM) algorithm [37]. Unfortunately, the LM quantization levels are non-uniformly spaced which makes it hard to design efficient arithmetic units to process such signals. Furthermore, for $B_y = 8$ as in Figure 4(b), LM achieves an $\text{SQNR}_{q_y(\text{dB})} = 41.31 \text{ dB}$ which is only 0.5 dB better than MPC. Thus, MPC offers a practical alternative to LM for assigning minimal precision to the column ADC in IMCs and the accumulator precision in digital architectures.

IV. ANALYTICAL MODELS FOR COMPUTE SNR

This section derives analytical expressions for SNR_a of a typical IMC. We introduce compute models that form the fundamental building blocks of IMCs and present analytical expressions for circuit domain equivalents of η_e and η_h in (6) for them. These are combined with algorithm and precision-dependent noise sources q_{iy} and q_y to obtain SNR_T . First, we show that most IMCs can be ‘explained’ via three in-memory compute models.

A. In-memory Compute Models

All IMCs are viewed as employing one or more *in-memory compute models* defined as a mapping of algorithmic variables y_o , x_j and w_j in (2) to physical quantities such as time, charge, current, or voltage, in order to (usually partially) realize an analog BL computation of the multi-bit DP in (2).

Furthermore, we suggest that most IMCs today employ one or more of the following three in-memory compute models

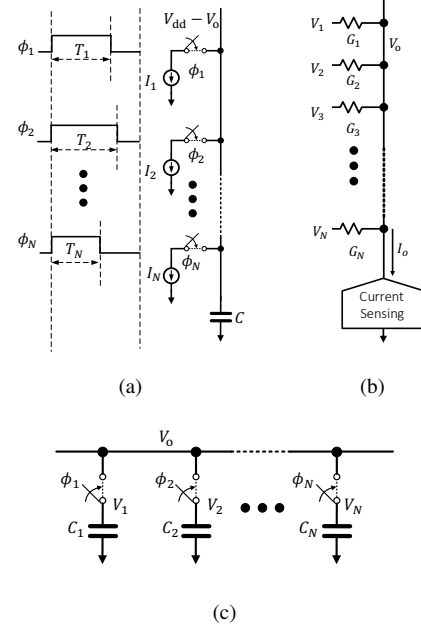


Fig. 5. In-memory compute models: (a) charge summing (QS), (b) current summing (IS), and the (c) charge redistribution (QR) model.

(see Fig. 5): (a) *charge summing* (QS) [5], [6], [9], [44]; (b) *current summing* (IS) [7], [11], [13], [38]; and (c) *charge redistribution* (QR) [6], [8], [9], [12], and conjecture that these compute models are in some sense universal in that they represent an approximation to a ‘complete set’ of practical, i.e., realizable, mappings of variables from the algorithmic to the circuit domain as shown in Table I.

Henceforth, we discuss the QS model and QR compute model and the corresponding IMC architectures referred to as QS-Arch, QR-Arch in detail since it is very commonly used. We also study compute-memory (CM) architectures [1], [6], [9] which combine the QS and QR compute models to implement a multi-bit DP.

Table II tabulates parameters of the QS and QR models in a representative 65 nm CMOS process. Table III summarizes the attributes of all three architectures.

B. Charge Summing (QS)

1) *The QS Model*: The QS model (see Fig. 5(a)) realizes the DP in (2) via the variable mapping ($y_o \rightarrow V_o$, $w_j \rightarrow I_j$, $x_j \rightarrow T_j$) where the cell current I_j is integrated over the WL pulse duration T_j ($j = 1, \dots, N$) on a BL (or cell) capacitor C resulting an output voltage as shown below:

$$(y_o \rightarrow V_o) = \frac{1}{C} \sum_{j=1}^N (w_j \rightarrow I_j)(x_j \rightarrow T_j) \quad (16)$$

where V_o is the DP output assuming infinite voltage headroom, i.e., no clipping. The cell current I_j depends upon transistor sizes and the WL voltage V_{WL} , and typical values are: C (a few hundred fFs), I_j (tens of μAs), and T_j (hundreds of ps).

Noise Models: The noise contributions in QS arise from the following sources: (1) variations in the pulse-widths T_j of

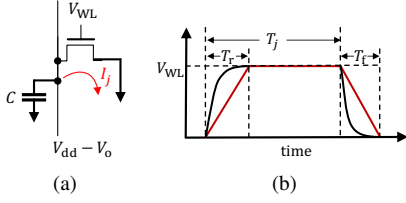


Fig. 6. Modeling the discharge process in the QS compute model: (a) cell current I_j , and (b) the word-line voltage pulse V_{WL} .

current switch pulses ϕ_j (Fig. 5(a)); (2) their finite rise and fall times (see Fig. 6(b)); (3) spatial variations in the cell currents I_j ; (4) thermal noise in the discharge RC-network; and (5) clipping due to limited voltage head-room. Thus, the analog DP output V_a corresponding to $y_a = y_o + \eta_a$ is given by:

$$\begin{aligned} (y_a \rightarrow V_a) &= (y_o \rightarrow V_o) + (\eta_e \rightarrow v_e) + (\eta_h \rightarrow v_c), \\ v_e &= v_\theta + \frac{1}{C} \sum_{j=1}^N i_j T_j + I_j(t_j - t_{rf}), \\ v_c &= \min(V_o, V_{o,\max}) - V_o, \end{aligned} \quad (17)$$

where $V_{o,\max}$ is the maximum allowable output voltage, and v_e and v_c are the voltage domain noise due to circuit non-idealities and clipping, respectively, $i_j \sim \mathcal{N}(0, \sigma_{I_j}^2)$ is the noise due to (spatial) current mismatch, and $t_j \sim \mathcal{N}(0, \sigma_{T_j}^2)$ is the noise due to (temporal) pulse-width mismatch, respectively, both of which are modeled as zero mean Gaussian random variables, t_{rf} models the impact of finite rise and fall times of the current switching pulses, and $v_\theta \sim \mathcal{N}(0, \sigma_\theta)$ is the integrated thermal noise voltage. Note: $V_{o,\max}$ can be as high as 0.9 V when $V_{dd} = 1$ V.

Analytical expressions to estimate the noise standard deviations σ_{I_j} , σ_{T_j} , σ_θ , and t_{rf} , (see appendix) are provided below:

$$\sigma_{I_j} = I_j \left(\frac{\alpha \sigma_{V_t}}{V_{WL} - V_t} \right) = I_j \sigma_D \quad (18)$$

$$t_{rf} = T_r - \left(\frac{V_{WL} - V_t}{V_{WL}} \right) \frac{T_r + T_f}{\alpha + 1} \quad (19)$$

$$\sigma_{T_j} = \sqrt{h_j} \sigma_{T_0}, \quad \sigma_\theta = \frac{1}{C} \sqrt{\frac{N T_{\max} g_m k T}{3}} \quad (20)$$

where σ_D^2 is normalized current mismatch variance, $T_j = h_j T_0$ is the delay of a h_j -stage WL driver composed unit elements with delay T_0 each, σ_{T_0} is the standard deviation of T_0 , T_r and T_f are WL pulse rise and fall times (see Fig. 6(b)), α is a fitting parameter in the α -law transistor equation, σ_{V_t} is standard deviation of V_t variations, k is the Boltzmann constant, T is the absolute temperature, and g_m is the transconductance of the access transistor.

Note that typically the WL voltage V_{WL} is identical for all rows in the memory array with a few exceptions such as [5] which modulate V_{WL} to tune the cell current I_j . The effects of rise/fall times and delay variations can be mitigated by carefully designing the WL pulse generators. Therefore, noise in QS is dominated by spatial threshold voltage variations. Indeed, using the typical values from Table II, we find that σ_{I_j}/I_j ranges from 8% to 25%, while σ_{T_j}/T_j ranges from 0.5% to 3%.

Energy and Delay Models: The average energy consumption

TABLE II
IN-MEMORY COMPUTE MODEL PARAMETERS IN A REPRESENTATIVE
65 nm CMOS PROCESS

	Parameter	Value	Parameter	Value
QS	k'	220 $\mu\text{A}/\text{V}^2$	α	1.8
	σ_{T_0}	2.3 ps	σ_{V_t}	23.8 mV
	$\Delta V_{BL,\max}$	0.8 V-0.9 V	V_{WL}	0.4 V – 0.8 V
	V_t	0.4 V	T_0	100 ps
QR	WLC_{ox}	0.31 fF	κ	0.08 fF ^{0.5}
	p	0.5		
Common Parameters				
	T	300 K	k	1.38e-23 JK ⁻¹
	V_{dd}	1 V	g_m	66 $\mu\text{A}/\text{V}$

in the QS model is given by:

$$E_{QS} = \mathbb{E}[V_a] V_{dd} C + E_{su} \quad (21)$$

where the spatio-temporal expectation $\mathbb{E}[V_a]$ is taken over inputs (temporal) and over columns (spatial) E_{su} is the energy cost of toggling switches ϕ_j s. Equation (21) shows that the energy consumption in the QS model increases with $C \propto$ array size, the supply voltage V_{dd} , and the mean value of the DP $\mathbb{E}[V_a]$.

The delay of the QS model is given by $T_{QS} = T_{\max} + T_{su}$, where T_{su} is the time required to precharge the capacitors and setup currents, and $T_{\max} = \max\{T_j\}$ is the longest allowable pulse-width.

2) *The QS Architecture (QS-Arch):* The charge summing architecture (QS-Arch) in Fig. 7(b) employs a 6T [41] or 8T [38] SRAM bitcell within the QS model (see Section IV-B). This architecture implements fully-binarized DPs on the BLs by mapping the input bit $\hat{x}_{i,j}$ to the WL access pulse $V_{WL,j}$ while the weights $\hat{w}_{i,j}$ are stored across B_w columns of the BCA so that the BC currents $I_{i,j} \propto \hat{w}_{i,j}$. The output $V_o = \Delta V_{BL}$ is the voltage discharge on the BL and the capacitance $C = C_{BL}$ is the BL capacitance in (16). QS-Arch sequentially (bit-serially) processes one multi-bit input vector \mathbf{x} in B_x in-memory compute cycles followed by a digital summing of the binarized DPs to obtain the final multi-bit DP (2).

We derive the analytical expressions of architecture-level noise models for QS-Arch using those of the QS model described in Section IV-B. In QS-Arch, clipping occurs in each of the $B_x \times B_w$ binarized DPs and contributes to the overall clipping noise variance $\sigma_{\eta_h}^2$ at the multi-bit DP output. Circuit noise from each binarized DP is aggregated to obtain the final circuit noise variance σ_e^2 . In addition, employing MPC imposed requirement on the final DP output precision B_y (15), we obtain the lower bound on ADC precision B_{ADC} .

Since the multi-bit DP computation in (2) is high-dimensional (N can be in hundreds), it is clear that the limited BL dynamic range e.g., $V_{o,\max}$ in (17), will begin to dominate SNR_a in (7). It is for this reason that most, if not all, IMCs resort to some form of binarization of the multi-bit DP in (2) prior to employing one of the in-memory compute models (see Table I). Ultimately, SNR_a limits the number and accuracy of BL computations per read cycle and hence the overall energy efficiency of IMCs.

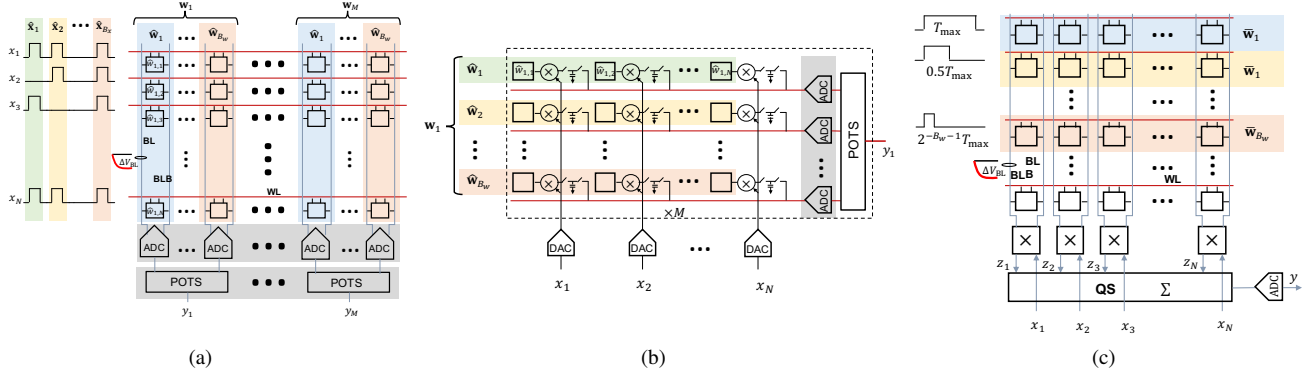


Fig. 7. Mapping of multi-bit DPs on in-memory architectures: (a) QS-Arch, (b) QR-Arch, and (c) CM.

TABLE III
DERIVED NOISE AND PRECISION PARAMETERS FOR QS-ARCH, QR-ARCH AND CM USING THE COMPOSITIONAL FRAMEWORK.

	QS-Arch	QR-Arch	CM
Bitcell type	6T or 8T	8T or 10T + MOM cap	6T
Analog Core Precision	Binarized ($B_w = B_x = 1$)	Binary-weighted ($B_w = 1$)	Multi-bit
Compute model used	QS	QR	QS & QR
Energy cost per DP	$E_{\text{QS-Arch}} = B_w B_x (E_{\text{QS}} + E_{\text{ADC}}) + E_{\text{misc}}$	$E_{\text{QR-Arch}} = B_w (E_{\text{QR}} + N E_{\text{mult}} + E_{\text{ADC}}) + E_{\text{misc}}$ $E_{\text{mult}} = \mathbb{E}[x_j(1 - w_j)] C_o V_{\text{dd}}$	$E_{\text{CM}} = 2N E_{\text{QS}} + E_{\text{QR}}$ $+ E_{\text{mult}} + E_{\text{ADC}} + E_{\text{misc}}$
Compute model mapping	$C \rightarrow C_{\text{BL}}$ $V_o \rightarrow \Delta V_{\text{BL}}$ $T_j \rightarrow T_{\text{WL},j}$	$C_j \rightarrow C_o$	QS: $C \rightarrow C_{\text{BL}}$ $V_o \rightarrow \Delta V_{\text{BL}}$ $T_j \rightarrow T_{\text{WL},j}$ QR: $C_j \rightarrow C_o$
$\sigma_{q_{iy}}^2$	$\frac{1}{12} N \Delta_x^2 \sigma_w^2 + \frac{1}{12} N \Delta_w^2 \mathbb{E}[x^2]$	$\frac{1}{12} N \Delta_x^2 \sigma_w^2 + \frac{1}{12} N \Delta_w^2 \mathbb{E}[x^2]$	$\frac{1}{12} N \Delta_x^2 \sigma_w^2 + \frac{1}{12} N \Delta_w^2 \mathbb{E}[x^2]$
$\sigma_{\eta_{\text{th}}}^2$	$\frac{4}{9} (1 - 4^{-B_w}) (1 - 4^{-B_x})$ $\sum_{k=k_h}^N (k - k_h)^2 \binom{N}{k} \left(\frac{1}{4}\right)^k \left(\frac{3}{4}\right)^{N-k}$	0	$\frac{1}{12} N \mathbb{E}[x^2] \sigma_w^2 k_h^{-2} 2^{2B_w}$ $(1 - 2k_h 2^{-B_w})_+^2$
$\sigma_{\eta_e}^2$	$\frac{N \sigma_D^2 (1 - 4^{-B_w}) (1 - 4^{-B_x})}{9}$	$\frac{2}{3} (1 - 4^{-B_w}) N \left(\frac{\mathbb{E}[x^2] \sigma_{C_o}^2}{C_o^2} + \frac{2\sigma_g^2}{V_{\text{dd}}^2} + \sigma_{\text{inj}}^2 \right)$	$\frac{2}{3} N \mathbb{E}[x^2] \left(\frac{1}{4} - 4^{-B_w} \right) \sigma_D^2$
B_{ADC}	$\geq \min \left(\frac{\text{SNR}_{\text{A(dB)}} + 16.2}{6}, \log_2(k_h), \log_2(N) \right)$	$\geq \min \left(\frac{\text{SNR}_{\text{A(dB)}} + 16.2}{6}, B_x + \log_2(N) \right)$	$\geq \frac{\text{SNR}_{\text{A(dB)}} + 16.2}{6}$
V_c	$\min \left(4\sqrt{3N} \Delta V_{\text{BL,unit}}, \Delta V_{\text{BL,max}}, N \Delta V_{\text{BL,unit}} \right)$	$8V_{\text{dd}} \sqrt{\frac{\mathbb{E}[x^2] + \sigma_x^2}{N}}$	$\frac{8\sigma_w 2^{B_w} \Delta V_{\text{BL,unit}} \sqrt{\mathbb{E}[x^2]}}{\sqrt{N}}$

$k_h = \frac{\Delta V_{\text{BL,max}}}{\Delta V_{\text{BL,unit}}}$; $\sigma_D = \frac{\sigma_I}{I}$ is the normalized standard deviation of the bit-cell current (18); $(x)_+ = \max(x, 0)$; $\sigma_{\text{inj}}^2 = \mathbb{E}[x^2] WLC_{\text{OX}}/C_o$.

C. Charge Redistribution (QR)

1) *The QR model:* The QR model (Fig. 5(c)) is commonly employed to perform the additions in (2). The multiplications in (2) are separately computed via charging/discharging capacitor C_j in proportion to the product $w_j x_j$ ($j = 1, \dots, N$) as in [8], [12], or by employing explicit multiplier circuits such as in [6], [9]. The N capacitors share charge via a sequence of switching events (see Fig. 5(c)) to generate the final voltage V_o given by:

$$(y_o \rightarrow V_o) = \frac{1}{\sum_j C_j} \sum_j C_j (w_j x_j \rightarrow V_j) \quad (22)$$

The capacitors C_j are typically metal-on-metal (MOM) capacitors with values ranging from 1 fF to 10 fF [6], [12].

Noise Models: Assuming MOM-based C_j s, the noise contributions in QR arise from: (1) capacitor mismatch [45]; (2) charge injection due to switching [46]; and (3) thermal noise. Unlike QS, and similar to IA, the QR model does not suffer from headroom clipping noise. Hence, the DP output V_a corresponding to y_a in (6) is given by:

$$(y_a \rightarrow V_a) = (y_o \rightarrow V_o) + (\eta_e \rightarrow v_e) \quad (23)$$

$$= \frac{1}{\sum_j (C_j + c_j)} \sum_j (C_j + c_j) (V_j + v_{\theta_j} + v_j)$$

where v_e is the voltage domain noise term due to circuit non-idealities corresponding to η_e in (6), v_j is the noise is due to charge injection, $c_j \sim \mathcal{N}(0, \sigma_{C_j}^2)$ is the capacitor mismatch, and $v_{\theta_j} \sim \mathcal{N}(0, \sigma_{\theta_j}^2)$ is the thermal noise. Furthermore,

expressions for the noise parameters in (23) can be derived as [45], [46]:

$$\sigma_{C_j} = \kappa \sqrt{C_j}, \quad v_j = p \frac{WLC_{ox}(V_{dd} - V_t - V_j)}{C_j}, \quad \sigma_{\theta,j} = \sqrt{\frac{kT}{C_j}} \quad (24)$$

where κ is a technology- and layout-dependent Pelgrom coefficient [45], $0 \leq p \leq 1$ is constant that depends on the layout of the switch transistor, C_{ox} is the gate oxide capacitance per unit area, and W and L are the width and length of the switch transistor. The effect of noise in the QR compute model can be minimized by increasing the capacitors sizes at the expense of energy consumption as seen from (25) below.

Energy and Delay Models: The average energy consumption in the QR model is given by:

$$E_{QR} = \sum_j \mathbb{E}[(V_{dd} - V_j)] V_{dd} C_j + E_{su} \quad (25)$$

where E_{su} includes energy cost for the switches $\phi_{j,s}$.

The delay of the QR model is given by: $T_{QR} = T_{share} + T_{su}$, where T_{share} is the time required for charge sharing to complete, and T_{su} is the time required to precharge the capacitors to the desired voltages V_j .

2) *The QR architecture (QR-Arch):* The QR-Arch, e.g., [8], in Fig. 7(c) employs a modified BC to include a capacitor C_o and additional switches for multiplication within the QR model. While works such as [8] employ the parasitic capacitances on the BL within the BC, an explicit MOM capacitor is assumed for simplicity. QR-Arch implements a binary weighted DP by storing the weights $\hat{w}_{i,j}$ across B_w rows of the BCA and by providing a multi-bit analog input x_j to the multiplier. The multiplication is implemented by first charging the capacitor C_o to a voltage proportional to x_j and then discharging it based on $\hat{w}_{i,k}$. Multiplication is followed by a QR operation across the rows so that the final voltage across the capacitors in each row is proportional to binary-weighted DP. Thus, the QR-Arch processes one multi-bit input vector \mathbf{x} in one in-memory compute cycle to compute binary-weighted DPs that are power-of-two (POT) summed digitally to obtain the final multi-bit DP (2).

The average energy per DP $E_{QR-Arch}$ (see Table III) includes E_{QR} (25) and E_{misc} which in turn includes the energy consumption of the DACs used for converting x_j into the analog domain. The energy cost of DACs are amortized since these are shared by multiple DPs computations.

Since the QR compute model does not suffer from headroom clipping, $\sigma_h^2 = 0$ and the lower bound on B_{ADC} is dictated solely by MPC. The primary analog noise contributors ($\sigma_{\eta_e}^2$) are the capacitor mismatch ($\sigma_{C_o}^2$), charge injection noise (σ_{inj}^2) in the switches, and thermal noise (σ_{θ}^2) as indicated in Table III. An alternative QR model [43], [47], [48] is to directly switch the bottom plate of the capacitors with binary outputs of the BC multiplies. Doing so leads to greater energy efficiencies and significant reduction in charge injection noise. The analysis presented in this section can be extended to such models as well.

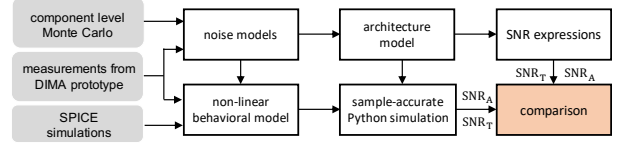


Fig. 8. SNR validation methodology.

D. Compute Memory

CM [1], [6], [9] in Fig. 7(c) employs a 6T SRAM BC within the QS (see Section IV-B) and QR (see Section IV-C) models. In the most general case, CM strives to implement a $B_w \times B_x$ -b DP directly by mapping B_x -b inputs x_j to pulse width T_j and/or amplitude $V_{WL,j}$ of the WL access pulses and storing B_w -b weights w_j in a column-major format across $B_w \times N$ cells. In practice, CM realizations such as [6] employ POT weighted WL access pulse-widths for B_w rows so that the voltage discharge ΔV_{BL} on the j -th BL is proportional to the weight w_j . The product $w_j x_j$ is realized using a per-column charge redistribution-based multiplier, followed by a QR stage to aggregate the N multiplier outputs. In this way, CM computes the $B_w \times B_x$ -b DP (2) in analog in a single in-memory compute cycle.

The energy cost per DP for CM in Table III is obtained by substituting $C = C_{BL}$ and $V_o = \Delta V_{BL}$ in (21), and using (25) with $C_j = C_o$. Here, E_{mult} is the energy consumption of the mixed-signal multiplier. The factor of 2 in first term accounts for discharge on both BL and BL-bar needed to realize signed weights [9]. The second term is the energy consumed in aggregating the column outputs using the QR model with identical capacitors C_o .

The expression for $\sigma_{\eta_e}^2$ neglects the impact of pulse width variations and other noise sources in QR since it is dominated by variations in the bit-cell current I_j . However, the sample-accurate Monte Carlo simulations incorporate all noise sources.

The factor of \sqrt{N} in the denominator of the expression for the ADC input range V_c due to the use of QR indicates that the loss in voltage range due to charge redistribution across N capacitors.

V. SIMULATION RESULTS

This section describes the SNR validation methodology for validating the SNR (noise) expressions in Table III and simulation results for QS-Arch.

A. SNR Validation Methodology

Figure 8 describes the SNR validation methodology. We obtain the QS and QR model parameters (Section IV) using Monte Carlo circuit simulations in a representative 65 nm CMOS process, with experimental validation of some of these, e.g., σ_{η_e} , from our IMC prototype ICs [6], [49] when possible.

Incorporating non-linear circuit behavior along with noise models, sample-accurate Monte Carlo Python simulations are employed to numerically calculate SNR values using ensemble averaged (over 1000 instances) statistics. We compare the SNR values obtained through sample-accurate simulations

with those obtained by evaluating the analytical expressions in Table III.

The quantitative results in subsequent sections employ the QS and QR model parameter values in Table II along with QS-Arch, QR-Arch, and CM energy and noise models from Table III. An SRAM BCA with 512 rows and $C_{BL} = 270$ fF is assumed throughout. Energy and accuracy is traded-off of by tuning V_{WL} in QS-Arch and CM, and by tuning C_o in QR-Arch. We assume zero mean signed weights w_j and unsigned inputs x_j drawn independently from two different distributions. We set $B_x = B_w = 6$ everywhere, unless otherwise stated, so that $\text{SQNR}_{q_{iy}(\text{dB})} = 38.9 \text{ dB} \gg \text{SNR}_{a(\text{dB})}$ and therefore $\text{SNR}_A \approx \text{SNR}_a$ from (10). Next, we show how SNR_A and SNR_T trade-off with N and B_{ADC} .

B. SNR Trade-offs in IMCs

1) *QS-Arch* : Figure 9(a) shows that the maximum achievable SNR_A increases with V_{WL} . Further, for a fixed V_{WL} , QS-Arch also exhibits a sharp drop in SNR_A at high values of $N > N_{\text{max}}$, e.g., $\text{SNR}_A \approx 19.6 \text{ dB}$ for $N \leq 125$ and then drops with increase in N . A key reason for this trade-off is that $\sigma_{\eta_h}^2$ decreases while $\sigma_{\eta_e}^2$ increases as V_{WL} is reduced (see Table III), and since $\sigma_{\eta_h}^2$ limits N and $\sigma_{\eta_e}^2$ limits SNR_A . Thus, by controlling V_{WL} , we can trade-off N_{max} with SNR_A . Specifically, N_{max} increases by $2\times$ for every 3 dB drop in SNR_A .

In QS-Arch, the minimum value of B_{ADC} (see Table III) depends upon the minimum of: 1) the MPC term (15); 2) the headroom clipping term; and 3) the small N case where BL discharge ΔV_{BL} has a finite number of discrete levels. Figure 9(b) shows that $\text{SNR}_T \rightarrow \text{SNR}_A$ of Fig. 9(a) when B_{ADC} is greater than the lower bound (circled) in Table III for different values of V_{WL} and N .

2) *QR-Arch* : QR-Arch demonstrates a clear energy-accuracy-area trade-off as seen in Fig. 10(a). Here, SNR_A improves with capacitor C_o size but at the expense of higher energy and area costs. For instance, increasing C_o from 1 fF to 3 fF and 9 fF leads to SNR_a improvements of $\sim 8 \text{ dB}$ and $\sim 12 \text{ dB}$, respectively.

Figure 10(b) shows that the expressions in Table III correctly predict the minimum value of ADC precision B_{ADC} and the input range V_c . MPC is demonstrated to greatly reduce the ADC precision requirements as for this example 6-8 bits suffice in order to maintain SNR_a . In contrast, if BGC were to be employed, $B_{\text{ADC}} = 12$ would have been assigned.

3) *Compute Memory*: Figure 11(a) shows that the quantization noise term $\sigma_{q_{iy}}^2$ reduces and the headroom clipping noise $\sigma_{\eta_h}^2$ increases as a function of B_w implying an SNR_a -optimal value for B_w , e.g., SNR_a peaks at $B_w = 6$ and $B_w = 7$ for $V_{WL} = 0.8 \text{ V}$ and $V_{WL} = 0.7 \text{ V}$, respectively.

Figure 11(a) also shows another interesting trade-off, this time between headroom clipping noise $\sigma_{\eta_h}^2$ and $\sigma_{\eta_e}^2$, e.g., when $B_w = 7$, SNR_a is dominated by η_e when $V_{WL} = 0.6 \text{ V}$ and by η_h when $V_{WL} = 0.8 \text{ V}$. Furthermore, both noise sources are balanced when $V_{WL} = 0.7 \text{ V}$. In fact, one can show that the clipping threshold k_h is proportional to σ_D indicating this relationship.

Figure 11(b) shows that choosing B_{ADC} using MPC (15) ensures that the SNR_T is indeed within 0.5 dB of SNR_a in Fig. 11(a). Once more, MPC assigns $B_{\text{ADC}} \leq 8$ when $B_x = B_w = 6$ and $N = 128$ which is much smaller than $B_{\text{ADC}} = 19$ determined via BGC.

C. Impact of ADC Precision

Minimizing the column ADC energy is critical to maintain IMC's energy efficiency. ADCs in IMCs need to operate in a noise-limited regime due to the high PAR of high-dimensional DP outputs combined with severe area constraints imposed by column-pitch matching requirements. To estimate the ADC energy costs we use the following empirical model based on [48]:

$$E_{\text{ADC}} = k_1 \left(B_{\text{ADC}} + \log_2 \left(\frac{V_{\text{DD}}}{V_c} \right) \right) + k_2 \left(\frac{V_{\text{DD}}}{V_c} \right)^2 4^{B_{\text{ADC}}} \quad (26)$$

where V_c is the voltage range that need to be quantized, and $k_1 = 100 \text{ fJ}$ and $k_2 = 1 \text{ aJ}$ are empirical parameters [48] based on the recent ADCs [50], [51].

From (26), it is clear that the energy consumption of ADC decreases with V_c and increases with B_{ADC} . If BGC is employed, then $2^{B_{\text{ADC}}} \propto N$ (12) resulting in ADC energy increasing with N when V_c is constant, as in the case of QR-Arch and in CM (see Fig 12(b) and Fig 12(c)). However, in QS-Arch, $V_c \propto N$ therefore the ADC energy consumption in QS-Arch remains constant with N (see Fig 12(a)).

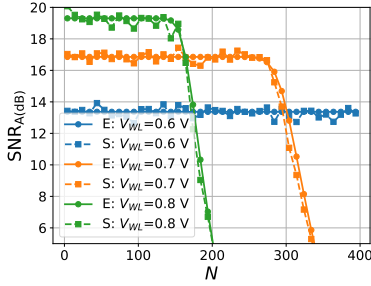
On the other hand, if MPC is employed, B_{ADC} remains constant with N (Table III), and hence E_{ADC} only depends on V_c . In QS-Arch, E_{ADC} reduces with N as $V_c \propto \sqrt{N}$, while in QR-Arch and CM E_{ADC} increases with N as $V_c \propto 1/\sqrt{N}$ (see Fig 12(a)). Note that for QR-Arch and CM, MPC leads to significant energy savings over BGC criterion since $E_{\text{ADC}} \propto N^2$ in BGC while $E_{\text{ADC}} \propto N$ using MPC.

D. Impact of Technology Scaling

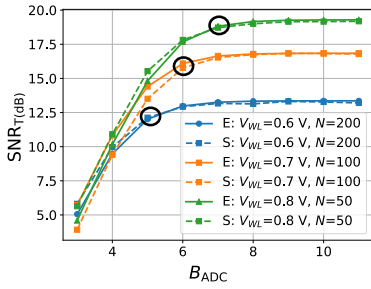
One expects IMCs to exhibit improved energy efficiency and throughput in advanced process nodes due to lower capacitance and lower supply voltage. However, the impact of technology scaling on the analog noise sources also needs to be considered. To study this trade-off, we employ the SNR and energy models from Section IV (see Table III) with parameters scaled as per the ITRS roadmap [52]. FDSOI technology is assumed for the 22 nm, 11 nm and 7 nm nodes.

For a specific node, Fig. 13 shows that the energy cost reduces by $2\times$ in CM and QS-Arch, and $4\times$ in QR-Arch for every 6 dB drop in SNR_a . QS-Arch suffers a catastrophic drop in SNR_a before reaching the input quantization noise limit set by (8). This drop occurs due to an increase in the clipping noise variance $\sigma_{\eta_h}^2$. In contrast, QR-Arch is able to approach quantization noise limits as it does not suffer from headroom clipping noise.

Across technology nodes, the maximum achievable SNR_A in QS-Arch and CM *reduces* as technology scales from 65 nm down to 7 nm due to: 1) increased clipping probability caused by lower supply voltages, and 2) increased variations in BL

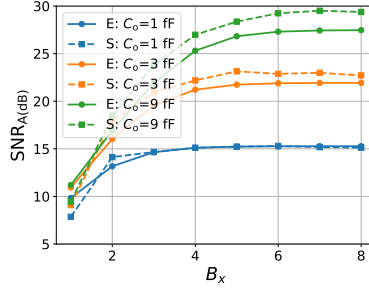


(a)

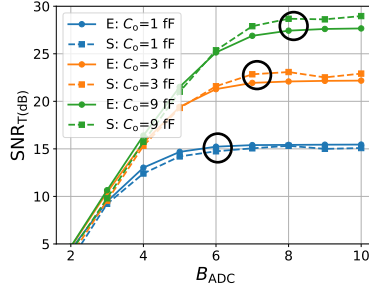


(b)

Fig. 9. SNR trade-offs in the QS-Arch with $B_x = B_w = 6$: (a) $\text{SNR}_{A(\text{dB})}$ vs. N for different values of V_{WL} , and (b) $\text{SNR}_{T(\text{dB})}$ vs. B_{ADC} showing that the expression in Table III correctly predicts the minimum ADC precision B_{ADC} (circled). Close match is achieved between expressions in Table III (E) and simulations (S) of (17).

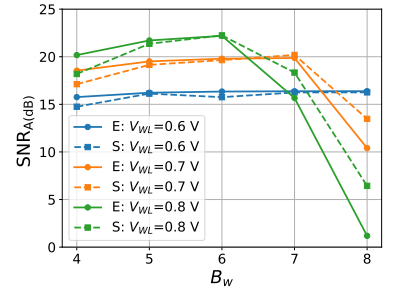


(a)

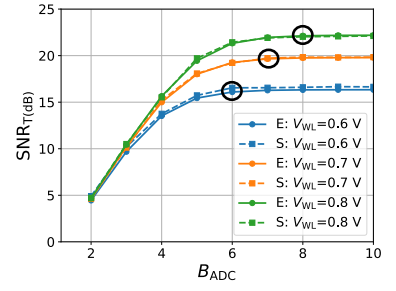


(b)

Fig. 10. SNR trade-offs in the QR-Arch with $B_w = 7$, and $N = 64$: (a) $\text{SNR}_{A(\text{dB})}$ as a function of B_x for different values of C_o showing that the SNR improves with C_o , and (b) $\text{SNR}_{T(\text{dB})}$ as a function of B_{ADC} for different values of C_o with $B_x = 6$ and $B_w = 7$, showing that the expression in Table III correctly predicts the minimum ADC precision B_{ADC} (circled). Here, 'E' and 'S' correspond to the evaluation of the expressions in Table III and sample-accurate simulations of (23), respectively.

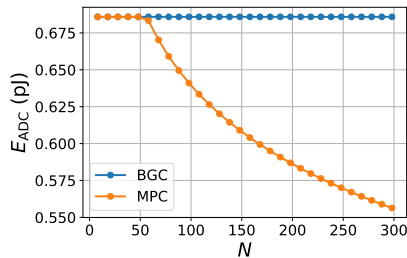


(a)

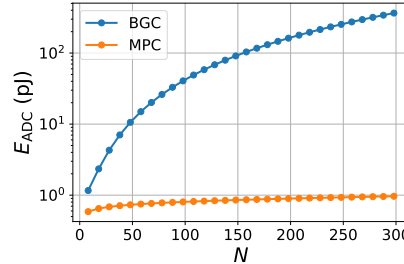


(b)

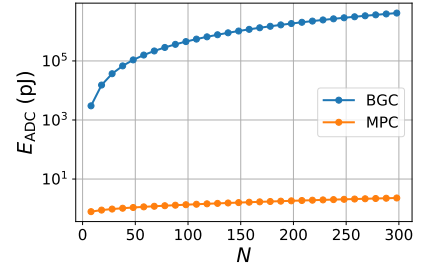
Fig. 11. SNR trade-offs in CM with $B_x = 6$ and $N = 128$: (a) $\text{SNR}_{A(\text{dB})}$ vs. B_w indicating the existence of an optimal value of B_w that balances quantization and headroom clipping noise, and (b) $\text{SNR}_{T(\text{dB})}$ vs. B_{ADC} with $B_w = 6$. Here, 'E' and 'S' correspond to the evaluation of the expressions in Table III and sample-accurate simulations using (17) and (23), respectively.



(a)

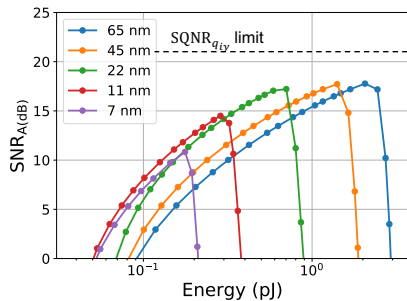


(b)

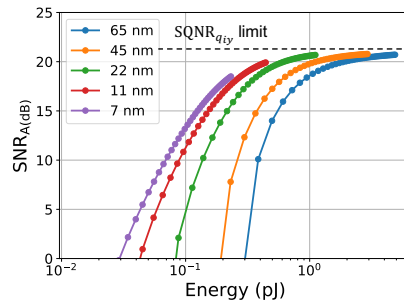


(c)

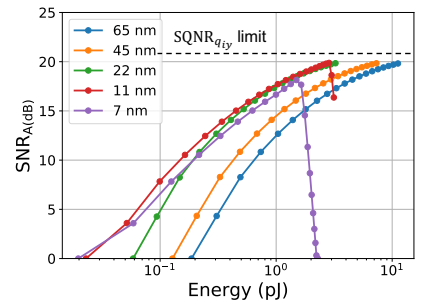
Fig. 12. ADC energy in (a) QS-Arch, (b) QR-Arch and (c) CM with $B_x = B_w = 6$ as a function of N when B_{ADC} chosen according to BGC (12), and the MPC criterion (Table III) such that $\text{SNR}_{T(\text{dB})}$ is within 0.5 dB of $\text{SNR}_{A(\text{dB})}$. $V_{\text{WL}} = 0.8$ V in CM, $V_{\text{WL}} = 0.7$ V in QS-Arch, and $C_o = 3$ fF in QR-Arch.



(a)



(b)



(c)

Fig. 13. Impact of CMOS technology scaling on the compute SNR vs. energy trade-off in (a) QS-Arch (swept parameter: V_{WL}), (b) QR-Arch (swept parameter C_o), and (c) CM (swept parameter: V_{WL}) with $B_x = 3$, $B_w = 4$, and $N = 100$.

discharge voltage ΔV_{BL} due to smaller V_{dd}/V_t ratio. As a result, Fig. 13 also shows that the energy consumption, *at the same* SNR_A , is in fact *higher* in 11 nm and 7 nm nodes as compared to the 22 nm node in QS-Arch and CM due to the need to employ a higher values of V_{WL} to control variations in ΔV_{BL} implying the technology scaling may not be friendly to IMCs based on the QS compute model.

VI. CONCLUSIONS AND SUMMARY

Based on the results presented in the earlier sections, we provide the following IMC design guidelines:

- For IMCs to be useful in realizing DNNs, the compute SNR of their analog core (SNR_a) needs to be the range 10 dB – 40 dB or greater depending on the layer. This is because the total SNR (SNR_T) of DP computations implemented on IMCs is upper bounded by SNR_a .
- In order for $SNR_T \rightarrow SNR_a$ with minimal energy and latency costs: 1) use (8) to ensure that the weight and activation precisions are sufficiently (e.g., 9 dB) below analog noise sources; and 2) use the MPC-based Precision Assignment Rule (15) to assign the ADC precision.
- QS-based architectures tend exhibit lower energy cost at low compute SNRs. Meanwhile, QR-based architectures are preferred when the compute SNR requirements are higher.
- For the QS-Arch, given an array size, there exists a trade-off between the maximum achievable SNR_a and the maximum realizable DP dimension N . Multi-bank IMCs will be required for high-dimensional DPs in order to boost the overall compute SNR.
- Technology scaling will have an adverse impact on the maximum achievable SNR_a and the energy cost incurred for a fixed SNR_a for both QS-Arch and CM.
- When MPC is employed, the ADC energy increases with the DP size N for both QR-Arch and CM due to the decreasing signal variance in the QR compute model. The opposite trend is observed for QS-Arch where the ADC energy decreases as N is increased.
- CM avoids incurring large ADC energy consumption by realizing multi-bit DPs instead of binarized ones.

An overarching conclusion of this paper is that the drive towards minimizing energy and latency using IMCs, runs counter to meeting the compute SNR requirements imposed by applications. This paper quantifies this trade-off through analytical expressions for compute SNR and energy-delay models. It is hoped that IMC designers will employ these models as they seek to optimize the design of IMCs of the future, including the use of algorithmic methods for SNR boosting such as statistical error compensation (SEC) [53].

APPENDIX A SQNR EXPRESSIONS

We present the derivation of the expressions of $SQNR_{q_{iy}}(\text{dB})$ in (8), $SQNR_{q_y}(\text{dB})$ in (9), $SQNR_{q_y}^{\text{BGC}}(\text{dB})$ in (13), and $SQNR_{q_y}^{\text{MPC}}(\text{dB})$ in (14).

Derivation of $SQNR_{q_{iy}}(\text{dB})$ in (8):

Substituting $\Delta_w = w_m 2^{-B_w+1}$ and $\Delta_x = x_m 2^{-B_x}$ in (5) yields:

$$\sigma_{q_{iy}}^2 = \frac{N}{3} \left(\sigma_w^2 \frac{x_m^2}{4} 2^{-2B_x} + \mathbb{E}[x^2] w_m^2 2^{-2B_w} \right) \quad (27)$$

which we substitute into the expression of $SQNR_{q_{iy}}$ in (7) along with the expression of $\sigma_{y_o}^2$ from (5) to obtain:

$$SQNR_{q_{iy}} = \frac{N \mathbb{E}[x^2] \sigma_w^2}{\frac{N}{3} \left(\sigma_w^2 \frac{x_m^2}{4} 2^{-2B_x} + \mathbb{E}[x^2] w_m^2 2^{-2B_w} \right)} \quad (28)$$

Dividing both numerators and denominators by $\frac{N}{3} \mathbb{E}[x^2] \sigma_w^2 2^{-2(B_x+B_w)}$, (28) can be written as:

$$SQNR_{q_{iy}} = \frac{3 \times 2^{2(B_x+B_w)}}{\zeta_x^2 \zeta_w^2 \left(\frac{2^{2B_x}}{\zeta_x^2} + \frac{2^{2B_w}}{\zeta_w^2} \right)} \quad (29)$$

The result for $SQNR_{q_{iy}}(\text{dB})$ in (8) follows by taking $SQNR_{q_{iy}}(\text{dB}) = 10 \log_{10}(SQNR_{q_{iy}})$, with $SQNR_{q_{iy}}$ given by (29).

Derivation of $SQNR_{q_y}(\text{dB})$ in (9):

From the SQNR definition in (1), we have

$$SQNR_{q_y}(\text{dB}) = 6B_y + 4.78 - \zeta_y(\text{dB})$$

Thus, it suffices to show that $\zeta_y(\text{dB}) = \zeta_x(\text{dB}) + \zeta_w(\text{dB}) + 10 \log_{10}(N)$ for the result in (1) to follow. For simplicity, let us assume signed inputs and weights. Since $y_o = \mathbf{w}^T \mathbf{x}$, we have $y_m = N x_m w_m$ (no clipping) and $\sigma_{y_o} = \sqrt{N} \sigma_x \sigma_w$. Thus, $\zeta_y = \frac{y_m}{\sigma_{y_o}} = \sqrt{N} \zeta_x \zeta_w$ with $\zeta_x = \frac{x_m}{\sigma_x}$ and $\zeta_w = \frac{w_m}{\sigma_w}$. The result follows by writing $\zeta_y(\text{dB}) = 20 \log_{10}(\zeta_y)$.

Derivation of $SQNR_{q_y}^{\text{BGC}}(\text{dB})$ in (13):

The result follows by replacing B_y in (9) by $B_x + B_w + \log_2(N)$ which is assigned by BGC as per (12). Note that $6 \log_2(N) \approx 20 \log_{10}(N)$ hence we obtain

$$\begin{aligned} SQNR_{q_y}^{\text{BGC}}(\text{dB}) &= 6(B_x + B_w + \log_2(N)) \\ &\quad - \zeta_x(\text{dB}) - \zeta_w(\text{dB}) - 10 \log_{10}(N) \\ &\approx 6(B_x + B_w) + 20 \log_{10}(N) \\ &\quad - \zeta_x(\text{dB}) - \zeta_w(\text{dB}) - 10 \log_{10}(N) \\ &= 6(B_x + B_w) - \zeta_x(\text{dB}) - \zeta_w(\text{dB}) + 10 \log_{10}(N) \end{aligned}$$

as listed in (13).

Derivation of $SQNR_{q_y}^{\text{MPC}}(\text{dB})$ in (14):

In MPC we have:

$$SQNR_{q_y}^{\text{MPC}} = \frac{\sigma_{y_o}^2}{\sigma_{q_y}^2 + p_c \sigma_{cc}^2} = \frac{\sigma_{y_o}^2}{\sigma_{q_y}^2 \left(1 + p_c \frac{\sigma_{cc}^2}{\sigma_{q_y}^2} \right)}$$

with $\sigma_{q_y}^2 = \frac{\Delta_y^2}{12} = \frac{y_c^2 2^{-2B_y}}{3}$, $p_c = \Pr\{|y_o| > y_c\}$, and $\sigma_{cc}^2 = \mathbb{E}[(y_o - y_c)^2 | |y_o| > y_c]$. The above can be re-written as

$$SQNR_{q_y}^{\text{MPC}} = \frac{3 \times 2^{2B_y}}{(\zeta_y^{\text{MPC}})^2 \left(1 + p_c \frac{\sigma_{cc}^2}{\sigma_{q_y}^2} \right)} \quad (30)$$

with $\zeta_y^{\text{MPC}} = \frac{y_c}{\sigma_{q_y}}$. The result for $SQNR_{q_y}^{\text{MPC}}(\text{dB})$ in (14) follows by taking $SQNR_{q_y}^{\text{MPC}}(\text{dB}) = 10 \log_{10}(SQNR_{q_y}^{\text{MPC}})$, with $SQNR_{q_y}^{\text{MPC}}$ given by (30).

APPENDIX B
ANALOG NOISE MODELS EXPRESSIONS

We present the derivation of expressions (18), (19), expressions for noise variances (η_h , η_e) and ADC input range V_c listed in Table III.

Derivation of (18):

Employ the α -law transistor I-V equation below to model the SRAM cell current I_j (see Fig. 6(a)):

$$I_j = \frac{W}{L} k' (V_{WL} - V_t)^\alpha \quad (31)$$

In the presence of threshold voltage variations, (31) transforms into:

$$I_j + i_j = \frac{W}{L} k' (V_{WL} - (V_t + v_t))^\alpha \quad (32)$$

where v_t is the threshold voltage variation and i_j is the resulting cell current variation. Using a 1st-order Taylor series expansion, we get:

$$i_j \approx v_t \frac{\partial I_j}{\partial V_t} = -v_t \frac{\alpha I_j}{V_{WL} - V_t} \quad (33)$$

Assuming v_t is a zero mean random variable with standard deviation $\sigma_{V_t} = \sqrt{\text{Var}(v_t)}$ leads to (18) with $\sigma_{I_j} = \sqrt{\text{Var}(i_j)}$.

Derivation of (19):

To model the impact of finite rise/fall time on the total voltage discharge associated with j -th cell $V_{o,j}$, we integrate the SRAM cell current over the wordline pulse window T_j to determine the total charge accumulated on the bitline cap C :

$$V_{o,j} + v_j = \frac{1}{C} \int_{t=0}^{t=T_j} I_j(t) dt \quad (34)$$

where $V_{o,j} = I_j T_j / C$ is the total discharge assuming an ideal V_{WL} pulse ($T_r = T_f = 0 \rightarrow I_j(t) = I_j$), and v_j is the voltage drop that accounts for these effects. Modeling the SRAM cell current as an ideal current source with value set by (31), we get:

$$V_{o,j} + v_j = \frac{Wk'}{LC} \int_{t=0}^{t=T_j} (V_{WL}(t) - V_t)^\alpha dt \quad (35)$$

To simplify the analysis, we employ a linear approximation (red curve) to a realistic V_{WL} waveform in Fig. 6(b). Evaluating (35) with the linear approximation results in:

$$V_{o,j} + v_j = \frac{I_j}{C} \left[T_j - T_r + \left(\frac{V_{WL} - V_t}{V_{WL}} \right) \frac{T_r + T_f}{\alpha + 1} \right] \quad (36)$$

Thereby obtaining (19) to account effect of rise and fall times of the WL pulse.

Derivation of (20) To derive the thermal noise variance in (20), we employ the bit-cell model in Fig 6(a). The access transistors in the j -th bitcell contributes thermal noise $i_{\theta,j}$. The final BL thermal noise voltage v_θ is obtained by integrating the thermal noise current ($i_{\theta,j}$) contributions from the N bit-cells attached to the BL, on the output capacitor C as follows:

$$v_\theta = \frac{1}{C} \sum_{j=1}^N w_j \left[\int_{t=0}^{t=T_j} i_{\theta,j} dt \right] \quad (37)$$

Assuming the access transistors are in saturation, the two-sided power spectral density of $i_{\theta,j}$ is given by $S_{i_\theta}(f) =$

$\frac{4}{3} g_m k T$. Therefore:

$$\mathbb{E} \left[\left(\int_{t=0}^{t=T_j} i_{\theta,j} dt \right)^2 \right] = T_j S_{i_\theta}(0) = T_j \frac{4}{3} g_m k T \quad (38)$$

We assume $T_j = x_j T_{\max}$ are independent and the integrated $i_{\theta,j}$ are independent and zero mean. Further, assuming $w_j \in \{0, 1\}$ are Bernoulli distributed with parameter 0.5, we obtain:

$$\sigma_\theta^2 = \mathbb{E}[v_\theta^2] = \frac{1}{C^2} \sum_{j=1}^N \mathbb{E}[w_j^2] \mathbb{E}[T_j] \frac{4}{3} g_m k T \quad (39)$$

$$= \frac{1}{C^2} \sum_{j=1}^N \frac{1}{2} \frac{T_{\max}}{2} \frac{4}{3} g_m k T = \left(\frac{T_{\max} N}{C^2} \right) \frac{g_m k T}{3} \quad (40)$$

Derivation of $\sigma_{\eta_h}^2$ in CM:

We write the headroom clipping noise in CM as:

$$\eta_h = \sum_{j=1}^N (w_j - \min(|w_j|, w_h) \text{sign}(w_j)) x_j = \boldsymbol{\lambda}^T \mathbf{x} \quad (41)$$

where $w_h = k_h \Delta_w$ is the smallest value of $|w_j|$ that leads to clipping, and $\boldsymbol{\lambda}$ is the clipping noise vector. The clipping noise terms can be assumed to be independent from each other and from the inputs. Furthermore, by virtue of the weights having a symmetric distribution, the clipping noise has zero mean, so that:

$$\sigma_{\eta_h}^2 = N \mathbb{E}[x^2] \mathbb{E}[\lambda^2]. \quad (42)$$

In addition, the headroom clipping noise term variance is given by:

$$\mathbb{E}[\lambda^2] = \Pr(|w| \geq w_h) \mathbb{E}[(w - w_h)^2 | |w| > w_h]$$

Then, we use the bound $\Pr(|w| \geq w_h) \leq \frac{\sigma_w^2}{w_h^2}$ by virtue of Chebyshev's inequality, and we evaluate $\mathbb{E}[(w - w_h)^2 | |w| > w_h] = \frac{(1-w_h)^2}{3}$. Substituting into the above, we obtain an estimate for the headroom clipping noise term variance:

$$\mathbb{E}[\lambda^2] \approx \frac{1}{12} \sigma_w^2 k_h^{-2} 2^{2B_w} (1 - 2k_h 2^{-B_w})_+^2 \quad (43)$$

which we plug into (42) to obtain the expression for the total clipping noise variance $\sigma_{\eta_h}^2$ in CM as listed Table III.

Derivation of $\sigma_{\eta_e}^2$ in CM:

We write the electrical noise in CM as: $\eta_e = \sum_{j=1}^N x_j \delta_{w_j}$ where δ_{w_j} is the electrical noise term corresponding to the discharge of weight w_j . By virtue of inputs being independent from electrical noise terms, and assuming the latter are identically distributed, we have:

$$\sigma_{\eta_e}^2 = N \mathbb{E}[x^2] \mathbb{E}[\delta_{w_j}^2]. \quad (44)$$

Next we derive $\mathbb{E}[\delta_{w_j}^2]$. Though CM uses both QS and QR compute models, the noise source from QR dominates. Specifically the noise due to current mismatch (18) dominates all other noise sources. In the presence of current mismatch noise, assuming the weight w_j is positive, the discharge on the j -th BL in CM is given by:

$$\Delta V_{BL_j} + \delta_{v_j} = \sum_{i=1}^{B_w-1} 2^{-i} T_{\max} \hat{w}_{i,j} (I_{i,j} + i_{i,j}) \quad (45)$$

where $i_{i,j}$ is the noise due to current mismatch with noise

variance given by (18), $T_{\max} = 2^{B_w-1}T_0$, and T_0 is the smallest WL pulse. Therefore, the effective weight represented the BL discharge is given by:

$$\begin{aligned} \frac{\Delta V_{\text{BL}j} + \delta_{v_j}}{2^{B_w-1}\Delta V_{\text{BL,unit}}} &= \sum_{i=1}^{B_w-1} 2^{-i}\hat{w}_{i,j} \left(1 + \frac{i_{i,j}}{I_{i,j}}\right) \\ &= w_j + \sum_{i=1}^{B_w-1} 2^{-i}\hat{w}_{i,j} \left(\frac{i_{i,j}}{I_{i,j}}\right) = w_j + \delta_{w_j} \end{aligned} \quad (46)$$

Note that the above equations assume w_j is positive, similar equations can be obtained if the weight is negative, where the discharge on BLB is considered instead of discharge on BL. Thus we obtain:

$$\mathbb{E}[\delta_{w_j}^2] = \sum_{i=1}^{B_w-1} 4^{-i}\mathbb{E}[\hat{w}_{i,j}^2]\sigma_D^2 \quad (47)$$

where $\sigma_D = \sigma_{I_j}/I_j$ (σ_{I_j} is obtained using (18)). Assuming weight bits are equally likely to be 0 or 1, the above simplifies to: $\mathbb{E}[\delta_{w_j}^2] = \frac{2\sigma_D^2}{3}(\frac{1}{4} - 4^{-B_w})$, which we plug into (44) to obtain the expression for $\sigma_{\eta_c}^2$ in CM as listed in Table III.

Derivation of V_c in CM:

In CM, BL discharge (45) is: $\Delta V_{\text{BL}} = 2^{B_w-1}V_{\text{BL,unit}}w_i$, and therefore after multiplications and aggregations via charge sharing voltage at the input of the ADC is given by:

$$\Delta V_o = \frac{2^{B_w-1}V_{\text{BL,unit}}}{N} \sum_i w_i x_i \quad (48)$$

Therefore, $V_c = 4\frac{2^{B_w}V_{\text{BL,unit}}}{N}\sigma_y$. Since $\sigma_y = \sqrt{N}\mathbb{E}[x^2]\sigma_w^2$, we obtain the expression for V_c in CM as listed in Table III.

Derivation of $\sigma_{\eta_h}^2$ in QS-Arch:

We write the headroom clipping noise in QS-Arch as:

$$\eta_h = \sum_{i=1}^{B_w} \sum_{j=1}^{B_x} 2^{1-i-j}\lambda_{i,j} \quad (49)$$

where $\lambda_{i,j}$ is the headroom clipping noise term for every bit-wise DP. Note that the nature of two's complement arithmetic makes the overall headroom clipping noise zero-mean in spite of the individual headroom clipping noise terms being non zero-mean. Further, cross-correlations of headroom clipping noise terms are neglected, so that the total headroom clipping noise variance is given by:

$$\sigma_{\eta_h}^2 = \sum_{i=1}^{B_w} \sum_{j=1}^{B_x} 4^{1-i-j}\mathbb{E}[\lambda_{i,j}^2]$$

In addition, for independent, identically distributed headroom clipping noise terms, we obtain:

$$\sigma_{\eta_h}^2 = \frac{4}{9}\mathbb{E}[\lambda^2](1 - 4^{-B_w})(1 - 4^{-B_x}) \quad (50)$$

where the clipping noise term is $\lambda = (y_{\text{BL}} - y_{\text{clip}})\mathbb{1}_{\{y_{\text{BL}} > y_{\text{clip}}\}}$ with y_{BL} being the discharge on a bit-line per bit-wise DP. Assuming weight and input bits to be independent and equally likely to be 0 or 1, we obtain that y_{BL} follows a binomial distribution $Bi(\frac{1}{4})$ so that:

$$\mathbb{E}[\lambda^2] = \sum_{k=k_h}^N (k - k_h)^2 \binom{N}{k} \left(\frac{1}{4}\right)^k \left(\frac{3}{4}\right)^{N-k}$$

which we plug into (50) to obtain the expression for $\sigma_{\eta_h}^2$ in QS-Arch as listed in Table III.

Derivation of $\sigma_{\eta_e}^2$ in QS-Arch:

We write the electrical noise in QS-Arch as:

$$\eta_e = \sum_{i=1}^{B_w} \sum_{j=1}^{B_x} \sum_{k=1}^N 2^{1-i-j}\delta_{i,j,k}$$

where $\delta_{i,j,k}$ is the electrical noise term due to circuit non-idealities which occurs when accessing the bit-cell at location (i,k) during the j^{th} cycle. By virtue of independence of electrical noise terms, we obtain the total electrical noise variance as

$$\sigma_{\eta_e}^2 = \sum_{i=1}^{B_w} \sum_{j=1}^{B_x} \sum_{k=1}^N 4^{1-i-j}\text{Var}(\delta_{i,j,k})$$

Further, for identically distributed electrical noise terms, the above simplifies to:

$$\sigma_{\eta_e}^2 = \frac{4}{9}N(1 - 4^{-B_w})(1 - 4^{-B_x})\text{Var}(\delta) \quad (51)$$

where δ is the electrical noise per bit-cell discharge whose variance is:

$$\text{Var}(\delta) = \frac{1}{4}\sigma_D^2,$$

with the $\frac{1}{4}$ term being due to the necessity of both input and weight bits to equal 1. This value of $\text{Var}(\delta)$ is plugged into (51) to obtain the expression for $\sigma_{\eta_e}^2$ in QS-Arch as listed in Table III.

Derivation of V_c in QR-Arch:

In QR-Arch, we estimate binary-weighted DP in each column using charge sharing, as: $V_i = \frac{V_{\text{dd}}}{N} \sum_j x_j w_{i,j}$. Since in V_i is the ADC input in QR-Arch we need its standard deviations to estimate V_c . Since $w_{i,j}$ is binary-valued, $\mathbb{E}[V] = V_{\text{dd}}E[x] = 0.5V_{\text{dd}}\mu_x$, and $\mathbb{E}[(V - 0.5V_{\text{dd}}\mu_x)^2] = \frac{V_{\text{dd}}^2}{4N}(2E[x_j^2] - \mu_x^2)$. Since $V_c = 8\sqrt{\mathbb{E}[V^2] - \mathbb{E}[V]^2}$, we obtain the expression for V_c in QR-Arch as listed in Table III.

REFERENCES

- [1] M. Kang *et al.*, "An energy-efficient VLSI architecture for pattern recognition via deep embedding of computation in SRAM," in *IEEE International Conference on Acoustics, Speech and Signal Processing (ICASSP)*, May 2014, pp. 8326–8330.
- [2] N. Shanbhag *et al.*, "Compute memory," US Patent 9,697,877, Issued July 4th 2017.
- [3] M. Kang *et al.*, *Deep In-memory Architectures for Machine Learning*. Springer, 2020.
- [4] N. Verma *et al.*, "In-memory computing: Advances and prospects," *IEEE Solid-State Circuits Magazine*, vol. 11, no. 3, pp. 43–55, 2019.
- [5] J. Zhang *et al.*, "In-memory computation of a machine-learning classifier in a standard 6T SRAM array," *IEEE Journal of Solid-State Circuits*, vol. 52, no. 4, pp. 915–924, April 2017.
- [6] M. Kang *et al.*, "A multi-functional in-memory inference processor using a standard 6T SRAM array," *IEEE Journal of Solid-State Circuits*, vol. 53, no. 2, pp. 642–655, 2018.
- [7] Z. Jiang *et al.*, "XNOR-SRAM: In-memory computing SRAM macro for binary/ternary deep neural networks," in *2018 IEEE Symposium on VLSI Technology*. IEEE, 2018, pp. 173–174.
- [8] A. Biswas and A. P. Chandrakasan, "Conv-RAM: An energy-efficient SRAM with embedded convolution computation for low-power CNN-based machine learning applications," in *IEEE International Solid-State Circuits Conference (ISSCC)*, 2018, pp. 488–490.
- [9] S. K. Gonugondla *et al.*, "A variation-tolerant in-memory machine learning classifier via on-chip training," *IEEE Journal of Solid-State Circuits*, vol. 53, no. 11, pp. 3163–3173, 2018.

- [10] H. Dbouk *et al.*, “KeyRAM: A 0.34 uJ/decision 18 k decisions/s recurrent attention in-memory processor for keyword spotting,” in *2020 IEEE Custom Integrated Circuits Conference (CICC)*. IEEE, 2020, pp. 1–4.
- [11] W.-S. Khwa *et al.*, “A 65nm 4Kb algorithm-dependent computing-in-memory SRAM unit-macro with 2.3 ns and 55.8 TOPS/W fully parallel product-sum operation for binary DNN edge processors,” in *IEEE International Solid-State Circuits Conference (ISSCC)*, 2018, pp. 496–498.
- [12] H. Valavi *et al.*, “A mixed-signal binarized convolutional-neural-network accelerator integrating dense weight storage and multiplication for reduced data movement,” in *2018 IEEE Symposium on VLSI Circuits*. IEEE, 2018, pp. 141–142.
- [13] J. Kim *et al.*, “Area-efficient and variation-tolerant in-memory BNN computing using 6T SRAM array,” in *2019 IEEE Symposium on VLSI Circuits*. IEEE, 2019, pp. 118–119.
- [14] Q. Dong *et al.*, “A 351 TOPS/W and 372.4 GOPS compute-in-memory SRAM macro in 7nm FinFET CMOS for machine learning applications,” in *IEEE International Solid-State Circuits Conference (ISSCC)*, 2020, pp. 242–243.
- [15] J.-W. Su *et al.*, “A 28nm 64Kb inference-training two-way transpose multibit 6T SRAM compute-in-memory macro for AI edge chips,” in *IEEE International Solid-State Circuits Conference (ISSCC)*, 2020, pp. 240–241.
- [16] X. Si *et al.*, “A 28nm 64Kb 6T SRAM computing-in-memory macro with 8b MAC operation for AI edge chips,” in *IEEE International Solid-State Circuits Conference (ISSCC)*, 2020, pp. 246–247.
- [17] A. Jaiswal *et al.*, “8T SRAM cell as a multi-bit dot product engine for beyond von-neumann computing,” *IEEE Transactions on Very Large Scale Integration (VLSI) Systems*, vol. 27, no. 11, pp. 2556–2567, 2019.
- [18] M. Ali *et al.*, “IMAC: In-memory multi-bit multiplication and accumulation in 6t sram array,” *IEEE Transactions on Circuits and Systems I: Regular Papers*, vol. 67, no. 8, pp. 2521–2531, 2020.
- [19] X. Si *et al.*, “A dual-split 6T SRAM-based computing-in-memory unit-macro with fully parallel product-sum operation for binarized DNN edge processors,” *IEEE Transactions on Circuits and Systems I: Regular Papers*, vol. 66, no. 11, pp. 4172–4185, 2019.
- [20] Z. Liu *et al.*, “NS-CIM: A current-mode computation-in-memory architecture enabling near-sensor processing for intelligent IoT vision nodes,” *IEEE Transactions on Circuits and Systems I: Regular Papers*, vol. 67, no. 9, pp. 2909–2922, 2020.
- [21] S. Zhang *et al.*, “A robust 8-bit non-volatile computing-in-memory core for low-power parallel MAC operations,” *IEEE Transactions on Circuits and Systems I: Regular Papers*, vol. 67, no. 6, pp. 1867–1880, 2020.
- [22] M. Gong *et al.*, “A 65nm thermometer-encoded time/charge-based compute-in-memory neural network accelerator at 0.735pJ/MAC and 0.41pJ/Update,” *IEEE Transactions on Circuits and Systems II: Express Briefs*, pp. 1–1, 2020.
- [23] A. Agrawal *et al.*, “Xcel-RAM: Accelerating binary neural networks in high-throughput SRAM compute arrays,” *IEEE Transactions on Circuits and Systems I: Regular Papers*, vol. 66, no. 8, pp. 3064–3076, 2019.
- [24] A. Jaiswal *et al.*, “i-SRAM: Interleaved wordlines for vector boolean operations using srams,” *IEEE Transactions on Circuits and Systems I: Regular Papers*, pp. 1–9, 2020.
- [25] S. Yin *et al.*, “Vesti: Energy-efficient in-memory computing accelerator for deep neural networks,” *IEEE Transactions on Very Large Scale Integration (VLSI) Systems*, vol. 28, no. 1, pp. 48–61, 2020.
- [26] S. Srinivasa *et al.*, “ROBIN: Monolithic-3D SRAM for enhanced robustness with in-memory computation support,” *IEEE Transactions on Circuits and Systems I: Regular Papers*, vol. 66, no. 7, pp. 2533–2545, 2019.
- [27] M. Abu Lebdeh *et al.*, “An efficient heterogeneous memristive XNOR for in-memory computing,” *IEEE Transactions on Circuits and Systems I: Regular Papers*, vol. 64, no. 9, pp. 2427–2437, 2017.
- [28] M. Kang *et al.*, “Deep in-memory architectures for machine learning - accuracy vs. efficiency trade-offs,” *IEEE Transactions on Circuits and Systems - Part I*, vol. 67, no. 5, pp. 1627–1639, January 2020.
- [29] S. K. Gonugondla *et al.*, “Fundamental limits on the precision of in-memory architectures,” in *IEEE/ACM International Conference on Computer-Aided Design (ICCAD)*, 2020.
- [30] C. Sakr *et al.*, “Analytical guarantees on numerical precision of deep neural networks,” in *International Conference on Machine Learning*, 2017, pp. 3007–3016.
- [31] C. Sakr and N. Shanbhag, “An analytical method to determine minimum per-layer precision of deep neural networks,” in *IEEE International Conference on Acoustics, Speech and Signal Processing (ICASSP)*, 2018, pp. 1090–1094.
- [32] I. Hubara *et al.*, “Binarized neural networks,” in *Advances in neural information processing systems*, 2016, pp. 4107–4115.
- [33] J. Choi *et al.*, “PACT: Parameterized clipping activation for quantized neural networks,” *arXiv preprint arXiv:1805.06085*, 2018.
- [34] S. Gupta *et al.*, “Deep learning with limited numerical precision,” in *International Conference on Machine Learning*, 2015, pp. 1737–1746.
- [35] A. S. Rekhi *et al.*, “Analog/mixed-signal hardware error modeling for deep learning inference,” in *Proceedings of the 56th Annual Design Automation Conference 2019*, ser. DAC ’19. New York, NY, USA: Association for Computing Machinery, 2019. [Online]. Available: <https://doi.org/10.1145/3316781.3317770>
- [36] S. Yin *et al.*, “XNOR-SRAM: In-memory computing SRAM macro for binary/ternary deep neural networks,” *IEEE Journal of Solid-State Circuits*, vol. 55, no. 6, pp. 1733–1743, 2020.
- [37] S. Lloyd, “Least squares quantization in pcm,” *IEEE Transactions on Information Theory*, vol. 28, no. 2, pp. 129–137, 1982.
- [38] X. Si *et al.*, “A twin-8T SRAM computation-in-memory macro for multiple-bit CNN-based machine learning,” in *IEEE International Solid-State Circuits Conference (ISSCC)*. IEEE, 2019, pp. 396–398.
- [39] H. Jia *et al.*, “A microprocessor implemented in 65nm CMOS with configurable and bit-scalable accelerator for programmable in-memory computing,” *arXiv preprint arXiv:1811.04047*, 2018.
- [40] S. Okumura *et al.*, “A ternary based bit scalable, 8.80 TOPS/W CNN accelerator with many-core processing-in-memory architecture with 896k synapses/mm²,” in *2019 IEEE Symposium on VLSI Circuits*. IEEE, 2019, pp. 248–249.
- [41] R. Guo *et al.*, “A 5.1pJ/neuron 127.3us/inference RNN-based speech recognition processor using 16 computing-in-memory SRAM macros in 65nm CMOS,” in *2019 IEEE Symposium on VLSI Circuits*. IEEE, 2019, pp. 120–121.
- [42] J. Yue *et al.*, “A 65nm computing-in-memory-based CNN processor with 2.9-to-35.8TOPS/W system energy efficiency using dynamic-sparsity performance-scaling architecture and energy-efficient inter/intra-macro data reuse,” in *IEEE International Solid-State Circuits Conference (ISSCC)*, 2020, pp. 234–235.
- [43] Z. Jiang *et al.*, “C3SRAM: An in-memory-computing sram macro based on robust capacitive coupling computing mechanism,” *IEEE Journal of Solid-State Circuits*, 2020.
- [44] M. Kang *et al.*, “An energy-efficient memory-based high-throughput VLSI architecture for convolutional networks,” in *IEEE International Conference on Acoustics, Speech and Signal Processing (ICASSP)*, May 2015.
- [45] V. Tripathi and B. Murmann, “Mismatch characterization of small metal fringe capacitors,” *IEEE Transactions on Circuits and Systems I: Regular Papers*, vol. 61, no. 8, pp. 2236–2242, 2014.
- [46] G. Wegmann *et al.*, “Charge injection in analog mos switches,” *IEEE Journal of Solid-State Circuits*, vol. 22, no. 6, pp. 1091–1097, 1987.
- [47] D. Bankman and B. Murmann, “An 8-bit, 16 input, 3.2 pJ/op switched-capacitor dot product circuit in 28-nm FDSOI CMOS,” in *Solid-State Circuits Conference (A-SSCC), 2016 IEEE Asian*. IEEE, 2016, pp. 21–24.
- [48] B. Murmann, “Mixed-signal computing for deep neural network inference,” *IEEE Transactions on Very Large Scale Integration (VLSI) Systems*, pp. 1–11, 2020.
- [49] S. K. Gonugondla *et al.*, “A 42pJ/decision 3.12 TOPS/W robust in-memory machine learning classifier with on-chip training,” in *IEEE International Solid-State Circuits Conference (ISSCC)*, 2018, pp. 490–492.
- [50] B. Murmann. (2019) ADC performance survey 1997-2019. [Online]. Available: <https://web.stanford.edu/~murmman/adcsurvey.html>
- [51] —, “A/D converter trends: Power dissipation, scaling and digitally assisted architectures,” in *2008 IEEE Custom Integrated Circuits Conference*. IEEE, 2008, pp. 105–112.
- [52] ITRS-collaborations, “ITRS roadmap tables,” *ITRS*, 2015. [Online]. Available: <http://www.itrs2.net/itrs-reports.html>
- [53] N. R. Shanbhag *et al.*, “Shannon-inspired statistical computing for the nanoscale era,” *Proceedings of the IEEE*, vol. 107, no. 1, pp. 90–107, 2018.